Available online at www.sciencedirect.com
ScienceDirect
International Journal of Heat and Mass Transfer 51 (2008) 3420–3433
International Journal of HEAT and MASS TRANSFER
www.elsevier.com/locate/ijhmt

Periodic bubble emission and appearance of an ordered bubble sequence (train) during condensation in a single microchannel

Wei Zhang [a,b], Jinliang Xu [a,*], John R. Thome [c]

[a] Micro Energy System Laboratory, Key Laboratory of Renewable Energy and Gas Hydrate, Guangzhou Institute of Energy Conversion, Chinese Academy of Sciences, Nengyuan Road, Wushan, Guangzhou 510640, PR China
[b] Graduate University of Chinese Academy of Sciences, Beijing 100039, PR China
[c] Laboratory of Heat and Mass Transfer, Ecole Polytechnique Fédérale de Lausanne, CH-1015 Lausanne, Switzerland

Received 9 January 2007; received in revised form 7 November 2007
Available online 8 January 2008

Abstract

Condensation of steam in a single microchannel, silicon test section was investigated visually at low flow rates. The microchannel was rectangular in cross-section with a depth of 30 μm, a width of 800 μm and a length of 5.0 mm, covered with a Pyrex glass to allow for visualization of the bubble formation process. By varying the cooling rate during condensation of the saturated water vapor, it was possible to control the shape, size and frequency of the bubbles formed. At low cooling rates using only natural air convection from the ambient environment, the flow pattern in the microchannel consisted of a nearly stable elongated bubble attached upstream (near the inlet) that pinched off into a train of elliptical bubbles downstream of the elongated bubble. It was observed that these elliptical bubbles were emitted periodically from the tip of the elongated bubble at a high frequency, with smaller size than the channel width. The shape of the emitted bubbles underwent modifications shortly after their generation until finally becoming a stable vertical ellipse, maintaining its shape and size as it flowed downstream at a constant speed. These periodically emitted elliptical bubbles thus formed an ordered bubble sequence (train). At higher cooling rates using chilled water in a copper heat sink attached to the test section, the bubble formation frequency increased significantly while the bubble size decreased, all the while forming a perfect bubble train flowing downstream of the microchannel. The emitted bubbles in this case immediately formed into a circular shape without any further modification after their separation from the elongated bubble upstream. The present study suggests that a method for controlling the size and generation frequency of microbubbles could be so developed, which may be of interest for microfluidic applications. The breakup of the elongated bubble is caused by the large Weber number at the tip of the elongated bubble induced by the maximum vapor velocity at the centerline of the microchannel inside the elongated bubble and the smaller surface tension force of water at the tip of the elongated bubble.

Keywords: Condensation; Microchannel; Microfluidics; Bubble train

1. Introduction

Condensation in microchannels could have many applications in miniature refrigeration systems. Nearly all theoretical and experimental work available in the public domain focus on channel sizes greater than 1 mm. Garimella et al. [1,2] reported the development of an experimentally validated model for pressure drop during intermittent flow for refrigerant R134a condensing in horizontal minichannels with hydraulic diameters ranging from 0.5 to 4.91 mm. A simple correlation for a non-dimensional unit-cell length based upon slug Reynolds numbers was used to compute the total pressure drop. Baird et al. [3] developed a new apparatus capable of controlling local heat fluxes through single small passages in thermoelectric coolers. They reported local heat transfer coefficients for condensation of R123 and R11 for a wide range of mass

* Corresponding author. Tel./fax: +86 20 87057656.
E-mail address: xujl@ms.giec.ac.cn (J. Xu).

0017-9310/$ - see front matter © 2007 Elsevier Ltd. All rights reserved.
doi:10.1016/j.ijheatmasstransfer.2007.11.025

Nomenclature

$\frac{dp}{dx}$	the axial pressure gradient of the vapor inside the elongated bubble (Pa/m)
D	the hydraulic diameter of the microchannel (m or μm)
D_x	horizontal axis length of elliptical bubble (μm)
D_y	vertical axis length of elliptical bubble (μm)
f	bubble emission frequency
G	mass velocity (kg/m^2 s or g/cm^2 s)
H_{in}	total enthalpy at the microchannel entrance (W)
H_{out}	total enthalpy at the microchannel exit (W)
h_f	saturated liquid enthalpy (J/kg)
h_v	saturated vapor enthalpy (J/kg)
Ja	Jakob number
L	the central microchannel length (m)
M	total mass flow rate (kg/s)
m_v	vapor mass flow rate near the exit of the central microchannel (kg/s)
Nu	Nusselt number
Pe	Peclet number
p_{in}	inlet pressure of the saturated water vapor (Pa or kPa)
R^*	reduced equivalent bubble radius
R_o	initial equivalent bubble radius after release from the elongated bubble (μm)
$R_{o,cir}$	optically measured initial biscuit-shaped bubble radius (μm)
R_{out}	equivalent biscuit-shaped bubble radius near the exit of the central microchannel (μm)
t	time (s or ms)
t_r	bubble residence time in the microchannel after its generation (s or ms)
T_{in}, T_{out}	inlet and outlet fluid temperature of the microcondenser (°C)
T_{w1}, T_{w2}	temperatures measured by thermocouples in the two holes of the copper heat sink (°C)
u_f	the axial velocity of the condensed water (m/s)
u_v	the axial velocity of the vapor inside the elongated bubble (m/s)
W	the width of the microchannel (m or μm)
We	Weber number
x	horizontal coordinate in the microchannel along the flow direction (μm)
$\bar{x}$	vapor mass quality near the exit of the central microchannel
y	vertical coordinate in the microchannel perpendicular to the flow direction (μm)
δ	microchannel depth (μm)
μ_v	the vapor viscosity (Pa s)
ρ_v	the vapor density (kg/m^3)
σ_f	the surface tension of condensed water (N/m)

velocities (70–600 kg/m^2 s) and heat fluxes (15–110 kW/m^2) in circular channels with internal diameters of 0.92 and 1.95 mm. They observed an enhancement in the condensation heat transfer coefficient for which the tube size had little or no influence. In another study of note, a theoretical model was proposed to estimate the film condensation heat transfer coefficient in square cross-section horizontal minichannels by Wang et al. [4]. Their model took into account the effects of surface tension, vapor shear stress and gravity. Their simulations were performed with R134a as the working fluid in a channel of 1.0 mm hydraulic diameter.

Médéric et al. [5] performed a flow visualization study on capillary condensation of *n*-pentane in a 0.56 mm glass channel at flow rates of 0–18 kg/m^2 s. They observed the oscillation of an elongated bubble formed at the entrance of their channel and also periodic break off of bubbles that flowed downstream. They deduced void fractions from image processing of their videos of the condensation process inside their capillary glass tube.

Cavallini et al. [6] studied the pressure drop characteristics of a 1.4 mm hydraulic diameter, multiport, minichannel tube during adiabatic two-phase flow of HFC refrigerants. The tube consisted of eleven parallel rectangular cross-section channels. Bandhauer et al. [7] developed a model to predict condensation heat transfer in circular microchannels and compared their predictions with their measured values. Recently, theoretical/numerical work on condensation heat transfer in microchannels has been presented by Du and Zhao [8] and Wang and Rose [9,10].

Up to now, very little information has been available on condensation in microchannels with a hydraulic diameter smaller than 100 μm. A recent study of condensation in microchannels was reported by Wu and Cheng [11] for channels having a hydraulic diameter of 82.8 μm where various flow patterns, such as fully droplet flow, droplet/annular/injection/slug-bubbly flow, annular/injection/slug-droplet flow, and fully slug-bubbly flow, were observed. They found that pressure and temperature oscillations correlated with these flow patterns.

In summary, most studies on condensation in microchannels have focused on: (a) channels with diameters about 1.0 mm in size or larger; (b) their two-phase pressure drops; (c) their condensation heat transfer coefficients and (d) the types of flow patterns formed.

With respect to the present study, there is ever increasing interest in controlling bubble and droplet size and frequency for microfluidic applications. Typical microfluidic channel sizes (height and width) are in the range of 10–100 μm, which are one to two orders of magnitude smaller than those often used for heat transfer engineering, e.g. in miniature refrigeration systems. The flow rates are in the range of 10–1000 nl/s. These parameters lead to nanoliter

size bubbles or droplets created at frequencies of 10 Hz–10 kHz and traveling at speeds from micrometers per second to centimeters per second (Mathieu and Armand [12]).

Normally, gas–liquid and liquid–liquid flows are characterized in terms of their Reynolds and capillary or Weber numbers [13]. It is interesting to control the droplet size of the dispersed phase and the speed at which the droplet moves relative to the continuous phase. Droplet flow can be created by mixing two streams of liquids, such as silicon oil and water. On the other hand, gas–liquid flow in microdevices can be used to focus columnar liquid samples (Huh et al. [14]). As summarized by Stone et al. [13], three microfluidic applications exploiting small bubbles or droplets were identified: (a) drivers for primary flows or mixed flows, (b) independent "chemical reactors" with very large surface area to volume ratio for each particle cluster, and (c) emulsion formation with a controlled droplet size distribution. For these applications, one need to understand the dynamics of the process, that is how small bubbles or droplets form, coalesce and breakup as well as what forces control changes to their shape, size and frequency. Unfortunately, not much is known about these phenomena at the microscale. Thus, the primary objective of the present study is to expound further on this topic.

For this study, a micro-condenser consisting of inlet and outlet plenums and a single microchannel were fabricated in silicon. The single microchannel had a width of 800 μm, a depth of 30 μm, and a length of 5 mm forming a planar microstructure and had a hydraulic diameter of 58 μm. By condensing saturated water vapor at the microchannel inlet, it was possible to control the emitted bubble shape, size, and frequency. The flow patterns in the microchannel generally consisted of a near stationary elongated bubble upstream near the inlet that broke up at its tip to form a bubble train flow downstream. The bubble train consisted of a set of isolated bubbles with uniform bubble size and constant speed relative to the continuous liquid phase. The bubbles had diameters in the range from tens to hundreds of microns, were generated at frequencies ranging from tens to thousands of Hertz, and flowed at constant speeds ranging from several to tens of centimeters per second. As the channel depth was 26.7 times less than the width and 166.7 times less than the length, any changes in depth contribute little to the overall movement of a bubble. It was also observed that the cooling rate strongly influenced the above parameters, with higher cooling rates (via flowing chilled water in the heat sink attached to the silicon test section) produced smaller bubble sizes and higher bubble detachment frequencies. The physical mechanisms behind these phenomena are described below.

2. Test section and experimental apparatus

2.1. Micro-condenser and copper heat sink

It is well known that "deep" microchannels act as large area fins, because the surface area to volume ratio is very large. However, flow visualization in deep microchannels is quite difficult and at present there are only two types of flow visualization systems capable of implementing this in microfluidic experiments: (1) stereo microscopes which allow the observation of bubble behavior and flow patterns in deep microchannels but cannot be used to accurately determine the bubble depth and (2) fluorescent microscopes, e.g. μ-PIV (Micro-Particle Image Velocimetry), which allow the bubble depth to be accurately determined, but have a very limited depth of field, i.e. the bubbles can only be viewed within a focal length (in this case depth) of several micrometers.

Alternatively, if a deep microchannel is rotated by 90°, the channel width and depth are interchanged and a wide, shallow channel results. The present silicon chip is designed based on this idea. Now, the bubble shape, size, position and emission frequency can be precisely obtained via analysis of a set of images.

Fig. 1 shows the micro-condenser test section assembly constructed for the present study where (a) shows the assembly in three-dimensions, (b) presents a vertical cross-sectional view of the assembly and (c) a top view of the silicon substrate. The silicon test section was fabricated using a silicon substrate with 400 μm thick and a pyrex glass plate was bonded to the silicon substrate as a cover for visualization purposes. In the silicon substrate, three successive zones were etched along the flow direction: the inlet plenum (acting as an inlet header), the single microchannel and the outlet plenum (acting as an outlet header). Both the inlet and outlet plenums have a cross-section that is 1000 μm wide and 120 μm deep. The microchannel is rectangular with a width of 800 μm, a depth of 30 μm and a length of 5000 μm. The microchannel has a large aspect ratio (width to depth) of 26.7. Because the channel is very shallow, the movement of a bubble is highly constrained in the z (vertical) direction. As shown in Fig. 1c, a two-dimensional coordinate system is indicated for the flow in the single microchannel; thus, the position and size of any bubble in the x–y plane can be measured at any time.

The top surface of the copper heat sink is in contact with the silicon micro-condenser and it has a planar area corresponding to that of the microchannel, i.e. 5000 × 800 μm. The silicon micro-condenser makes good thermal contact with the copper heat sink using a thin layer of thermally conductive silver paste. Water flowing through the interior of the copper heat sink cools the base of the micro-condenser and condenses the vapor inside the microchannel (see Fig. 1b). Two fine thermocouple wires (T_{w1}, T_{w2}) are inserted into two holes in the copper heat sink in order to measure the temperature at those two points (see Fig. 1b). The two cooling modes used will be described below.

2.2. Experimental setup

As shown in Fig. 2, the experimental test loop consists of four subsystems: the pressure and temperature

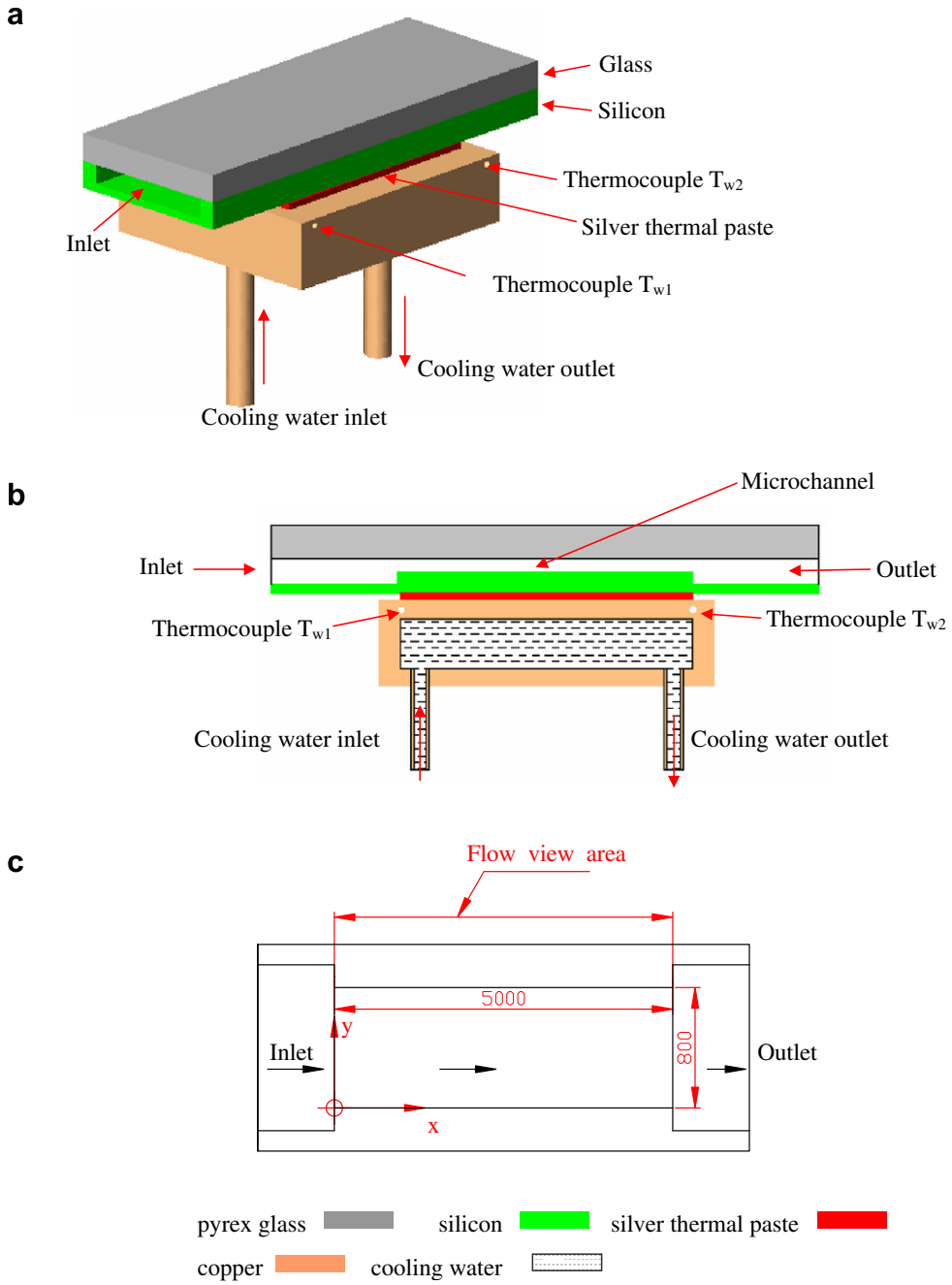

Fig. 1. The silicon microchannel condenser assembly (all dimensions in microns).

controlled steam generator, the micro-condenser test section with its copper heat sink, the microscope and high speed camera for flow visualization, and the mass balance for flow rate measurement. The steam generator and the micro-condenser are connected by a flexible capillary tube. A 2 μm filter, pressure transducer and small thermocouples were installed successively along the capillary tubes connecting the steam generator to the test section and the electronic balance. The vapor temperature at the microchannel inlet is measured by the thermocouple placed as close to the micro-condenser as possible. The capillary tube was connected to the micro-condenser using a carefully designed miniature adapter. In order to avoid vapor condensation inside the capillary tube, a small diameter metal wire was wrapped around the outside of it and used as a heater (powered by an adjustable AC power supply). The capillary tube was further wrapped with a thermally insulating material.

To operate the system, initially degassed and deionized water is stored in the steam generator which has an electric heater at its bottom. The AC power unit supplies current to the heater to evaporate the water, operating in conjunction with a temperature control unit using a PID mode. A high precision pressure transducer and safety

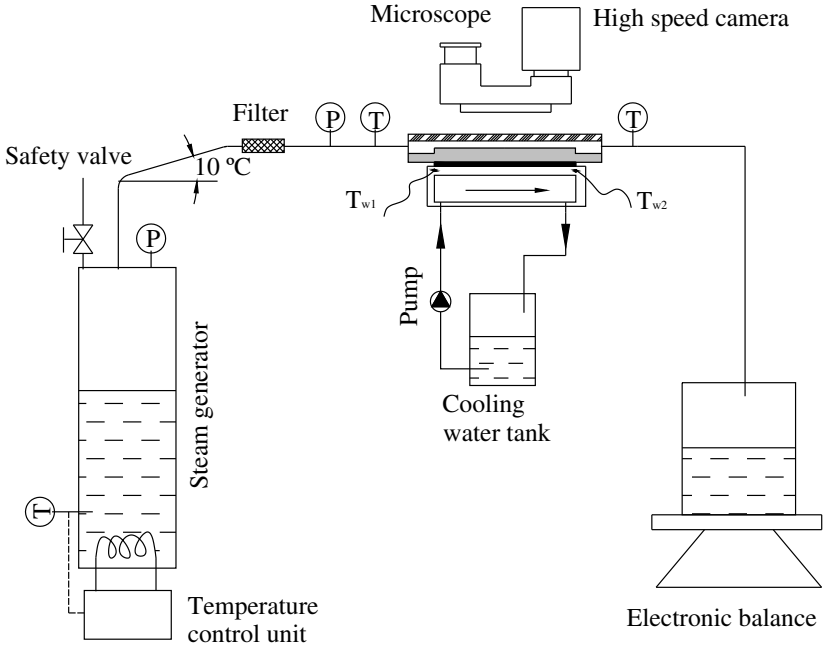

Fig. 2. Experimental setup.

valve are installed at the top of the steam generator pressure tank. The safety valve is set at the desired pressure value for operation. When the desired pressure is attained inside the steam generator, the safety valve automatically opens to discharge water vapor (and initially any additional air that has to be removed from the liquid before the tests) through an auxiliary capillary tube to a cold liquid pool (not shown in Fig. 2) where the exit of the capillary tube is placed below the surface of the pool. The discharged water vapor is rapidly condensed by the subcooled liquid while the air is not. This vapor/air discharge process is stopped by manually turning off the safety valve and checking to see when no more air bubbles are seen coming out of the liquid pool. Under these conditions the water in the steam generator is known to be completely degassed, indicated also by the fact that the water pressure and temperature inside the steam generator tank correspond very closely to the saturated state. For this, the liquid temperature was measured by a *K*-type jacketed thermocouple which is installed on the side wall of the pressure tank (see Fig. 2). In this way, only pure saturated water vapor without any non-condensable gas reaches the inlet plenum of the micro-condenser in the subsequent tests.

A closed loop pumping circuit was used to circulate chilled water between the cooling tank and the heat sink. Two cooling modes for the microchannel test section were used during the tests:

- Natural convection to the surrounding air with the ambient temperature maintained at 20 °C during the entire experiment (without flow of water to the copper heat sink).
- Forced convection by flowing water at 0 °C through the heat sink (ice and liquid water coexist in the cooling tank during the entire experiment to maintain a steady state).

Because the mass flow rate through the microchannel is so small, typically on the order of nanoliters per second, the remaining vapor is completely condensed and subcooled in the capillary tube downstream from the micro-condenser (not shown in Fig. 2). The liquid is collected in a beaker and its mass is weighed with an electronic balance of high precision to determine its flow rate.

2.3. Instrumentation, measurements and uncertainties

The inlet and outlet fluid temperatures, T_{in} and T_{out}, were measured by *K*-type jacketed thermocouples with an accuracy of 0.3 °C. The uncertainty in the liquid mass measurement is 0.02 g. The inlet pressure is measured by a Senex pressure transducer with an accuracy of 0.1% FS. The outlet pressure of the micro-condenser is equal to that of the ambient environment. This is because the cross-sectional area of the connected capillary tube downstream of the micro-condenser is two orders larger than that of the micro-condenser thus the pressure drop downstream of the micro-condenser can be neglected. The response time is 0.01 s for the pressure transducer and 0.1 s for the small diameter thermocouples (0.2 mm) used in this study. The pressure and temperature signals were recorded by a high speed data acquisition system (DL 750, Yokogawa, Inc., Japan) with 16 channels. While data sampling rates up to 10 million points per second were possible with this system, in the present study the recording rate is selected as 100

samples per second, which is fast enough to match the response times of the pressure and temperature signals.

A high speed camera was incorporated into a stereo microscope for the flow visualization. It was connected by a one inch *C*-type port. The microscope is a Leica M stereo microscope (Germany). The high speed camera is an X-stream Vision Xs-4 (IDT Inc., USA) which has a recording rate up to 5130 frames per second with a maximum resolution of 512 × 512 pixels. For the present study, recording rates of 4000–5000 frames per second and a resolution of 512 × 512 pixels were used during visualization, which was sufficient for the dynamic bubble behavior observed in the present tests. The field of view for condensation in the microchannel had an area of 5000 × 800 μm which corresponds to a resolution of 433 × 69 pixels; this results in an uncertainty in the identification of the location of the bubble interface of about 11 μm.

2.4. Test conditions

The test matrix in the present study covered the following range of parameters: inlet pressures from 115.84 to 288.49 kPa, inlet temperatures from 102.5 to 131.1 °C and mass fluxes from 140.7 to 818.5 kg/m^2 s. The mass fluxes were computed using the microchannel cross-sectional area of 800 × 30 μm.

During all experimental runs, the fluid pressure and temperature and the copper heat sink temperatures (T_{w1} and T_{w2}) were stable over time, which is not always the case for two-phase heat transfer in microchannels (especially with boiling). There were two reasons for achieving the high stability of these values in the present tests: (1) the transient flow patterns on the millisecond timescale do not affect the fluid states at the inlet and outlet and (2) the flow visualization with the high speed camera permits much greater resolution in time measurement compared to pressure and temperature. In other words, the fluid pressure and temperature signals do not see high frequency oscillations on the order of 1000 Hz. This behavior is similar to that of microscale boiling on the millisecond timescale which has been reported in a previous study (Xu et al. [15]).

Totally we performed the experiments for 24 runs. Table 1 only shows the runs that involved in the present paper, in which p_{in} and T_{in} are the pressures and temperatures at the entrance of the inlet plenum of the silicon chip, respectively, G is the mass flux in the central microchannel, q is the estimated heat flux due to the condensation heat transfer in the central microchannel. The computation of q is given as follows. The mass flow rate of the vapor phase near the exit of the central microchannel is $m_v = \rho_v \pi R_{out}^2 \delta f$, where R_{out} is the equivalent bubble radius at the microchannel exit, f is the bubble emission frequency. Thus the vapor mass quality is $\bar{x} = \rho_v \pi R_{out}^2 \delta f / M$, where M is the total mass flow rate. The total enthalpy at the central microchannel exit is $H_{out} = M(\bar{x}h_v + (1-\bar{x})h_f)$. Thus the estimated heat flux is computed as

$$q = \frac{H_{in} - H_{out}}{L \cdot W} = \frac{M[h_v - (\bar{x}h_v + (1-\bar{x})h_f)]}{L \cdot W} \quad (1)$$

It is shown in Table 1 that q is large. This is due to the enhanced condensation heat transfer by the larger temperature difference between the vapor phase and the chilling water in the copper heat sink. The heat flux estimation is helpful to understand at what condition the present phenomenon takes place.

Table 1
The run cases that involved in the present paper

Run	p_{in} (kPa)	T_{in} (°C)	T_{w1} (°C)	T_{w2} (°C)	G (g/(cm^2 s))	q (W/cm^2)
1	115.84	102.5	69.9	69.2	17.33	235
2	124.45	104.0	75.8	75.2	20.52	278
3	138.39	107.6	80.7	80.3	23.05	313
4	150.08	110.3	83.5	83.3	25.52	348
5	151.35	110.3	82.6	82.1	38.47	528
21	135.32	107.2	38.5	37.3	41.89	570
22	148.21	109.8	49.5	48.7	43.21	589
23	183.58	116.4	56.5	55.9	48.84	668
24	212.35	121.1	62.3	62.2	63.03	864

3. Results and discussion

3.1. General description of flow patterns in the microchannel

In general, there are two types of flow patterns in the microchannel as shown in Fig. 3. The main flow pattern is a stable (essentially static) elongated bubble upstream followed by an ordered bubble sequence (train) (refer to runs 1, 2, 3, 4, 21, 22, 23, and 24). Another flow pattern observed is annular flow when the inlet pressure of the saturated vapor is sufficiently high, such as for run 6 shown in Fig. 3.

Higher inlet pressures of the saturated vapor lead to the longer elongated bubble at the microchannel upstream (refer to Fig. 3) and higher flow rates. The cooling rate strongly affected the bubble shapes and sizes. In general, lower cooling rates with natural air convection (no flowing water in the heat sink) yield elliptical bubbles of larger size in the microchannel. Alternatively, higher cooling rates via flowing chilled water in the heat sink strongly enhanced the bubble emission frequency and produced smaller size bubbles. Bubble train flows showed isolated circular bubbles which remained constant in shape. The bubble flow patterns are described in the next section.

It should be noted that the present microchannel geometry plays an important role for the formation of the upstream elongated bubble. The inlet plenum (see Fig. 1) is wider and deeper than the central microchannel. The mass flux in the inlet plenum is only 20% of that in the central microchannel with the cross-section of 800 × 30 μm. Under such circumstance, a quasi-stable elongated bubble can be formed due to the surface tension force when the vapor flows across the junction interface from the inlet ple-

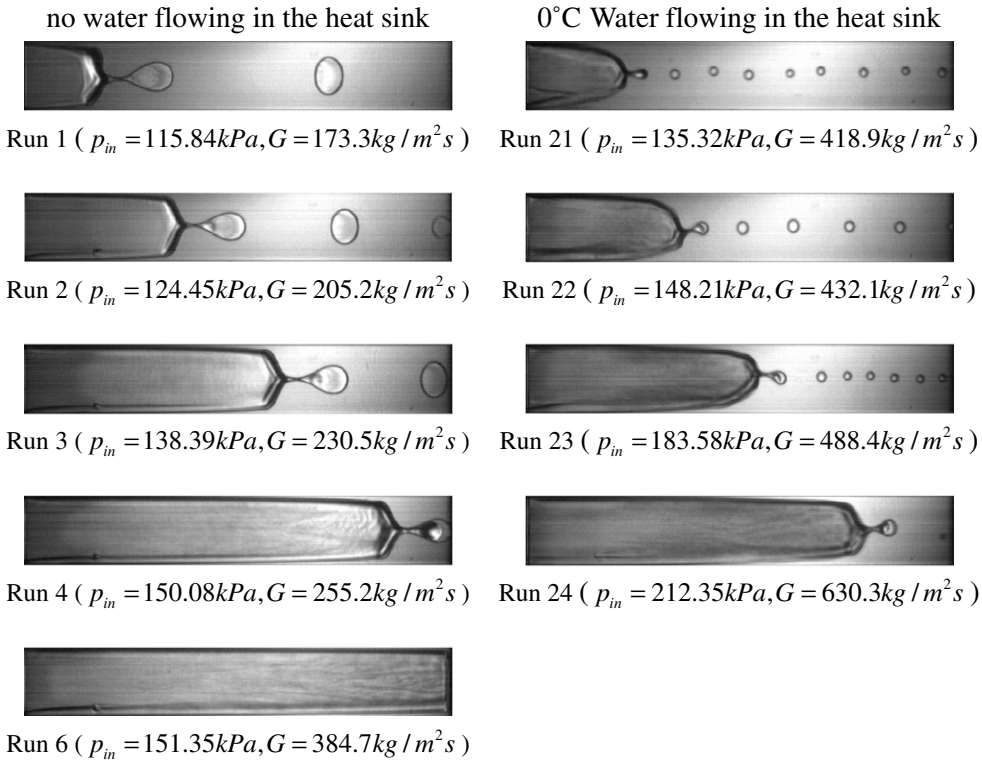

Fig. 3. Effect of saturated vapor inlet pressure and cooling rates on flow patterns in the microchannel (left column is for natural air convection cooling and right column is for forced convection via flowing chilled water in the copper heat sink).

num to the central microchannel. The inlet pressure is mainly overcome by the surface tension force due to the curvature interface of the elongated bubble.

3.2. Flow pattern with natural air convection cooling

The flow pattern with air natural convection heat transfer displays an elongated bubble surrounded by a thin film of condensate followed by a bubble train. The bubble train contains a set of isolated, elliptical bubbles which are periodically generated and suddenly appear and detach from the tip of the elongated bubble. Two modes of bubble generation (type 1 and 2) were found and are indicated in Fig. 4a and b by the dashed circles A and B. The first type of bubble generation mode is complex and has the following fluid structures: (1) concave front of the elongated bubble; (2) vapor necks; (3) droplet surrounded by the vapor; (4) bubble being emitted. The second type of bubble generation mode is simpler: a vapor neck is formed that connects the elongated bubble and the new small bubble to be emitted and once this neck stretches, thins and then breaks, the new bubble fully separates from the elongated bubble. Normally during both of these processes, the original elongated bubble remains stably attached to the inlet of the micro-evaporator channel. The concave front of the elongated bubble shown in Fig. 4a is formed by the surface tension of the droplet that is just downstream of the elongated bubble. Any bubbles in the microchannel should have three-dimensional shape. Generally the bubble is protruding in the channel depth direction. However, the bubble shape in such direction can not be easily visualized by the video camera system because the channel depth is so small.

The breakup of the elongated bubble is quite sensitive to the instantaneous state of the bubble tip. If the elongated bubble tip contains less vapor content, the breakup of the elongated bubble may take place at two points that deviate from the exact centerline of the microchannel simultaneously, referred to the first emission mode (see Fig. 4a). However, if much vapor content exists at the tip of the elongated bubble, the breakup point occurs exactly at the centerline of the microchannel, corresponding to Fig. 4b. For a specific run sharing the same inlet pressure and cooling rate, the dynamics of the isolated bubble formation from the elongated bubble repeats cycle by cycle. Some cycles have the first mode of bubble emission with an emission frequency, but some cycles possess the second mode of bubble emission with another frequency. This behavior will be described later. Such process may happen for the condensation flow in flattened but shallow microchannels such as the present case.

Once a new bubble separates from the elongated bubble, it is elliptical in shape (see Fig. 4c and d). Two parameters are sufficient to quantify the size of such an elliptical bubble: the lengths of the horizontal (D_x) and vertical (D_y) axes. Just after separation of the bubble, D_x is larger than D_y (see Fig. 4c). The ratio of D_x/D_y gradually changes due to the combined effects of inertia, viscosity and surface tension. At one point in time, $D_x = D_y$ and the bubble appears

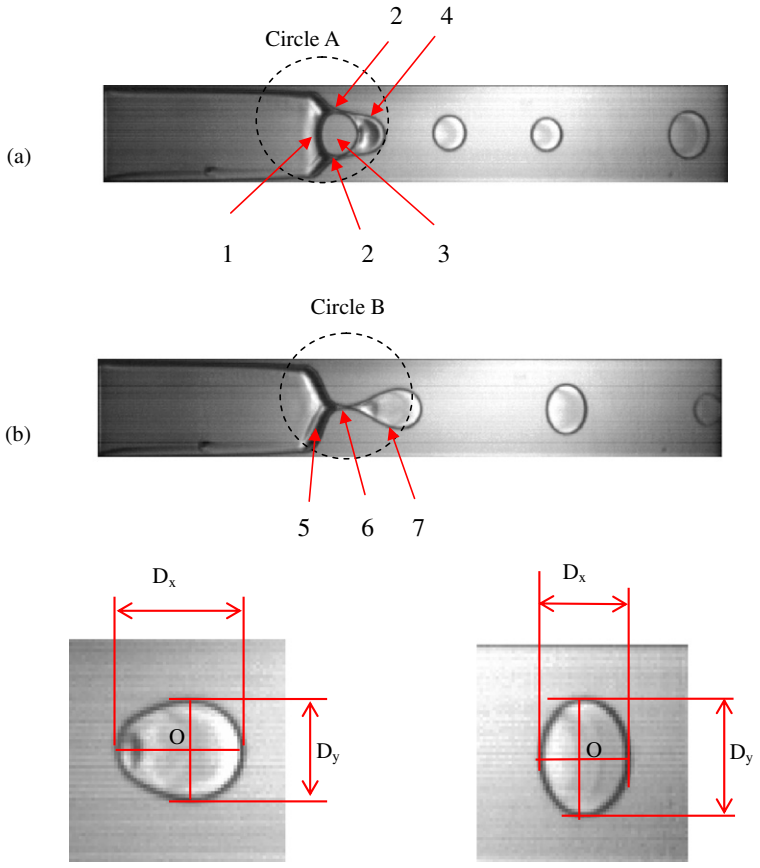

(c) horizontal elliptical bubble with $D_x > D_y$ (d) vertical elliptical bubble with $D_x < D_y$

Fig. 4. Video images taken for two different modes of bubble emission (first type (a) and second type (b)) and bubble shape after its generation: (1) concave front of the elongated bubble; (2) vapor necks; (3) droplet surrounded by the vapor; (4) bubble being emitted; (5) protruding front of the elongated bubble; (6) vapor neck; (7) detaching small bubble.

circular in our plane of view, but the bubble shape continues to change until a stable elliptical bubble forms with the vertical axis longer than the horizontal axis, $D_x < D_y$, (see Fig. 4d).

Periodic bubble formation from the elongated bubble occurs in the millisecond timescale. Fig. 5a and b show bubble trains forming in the microchannel from both generation modes for the same run 2. A bubble is first formed from the tip of the elongated bubble and then completely separates from it at $t = 1$ ms (see Fig. 5a).

Once a bubble is fully separated from the tip of the elongated bubble, the front of the elongated bubble gradually

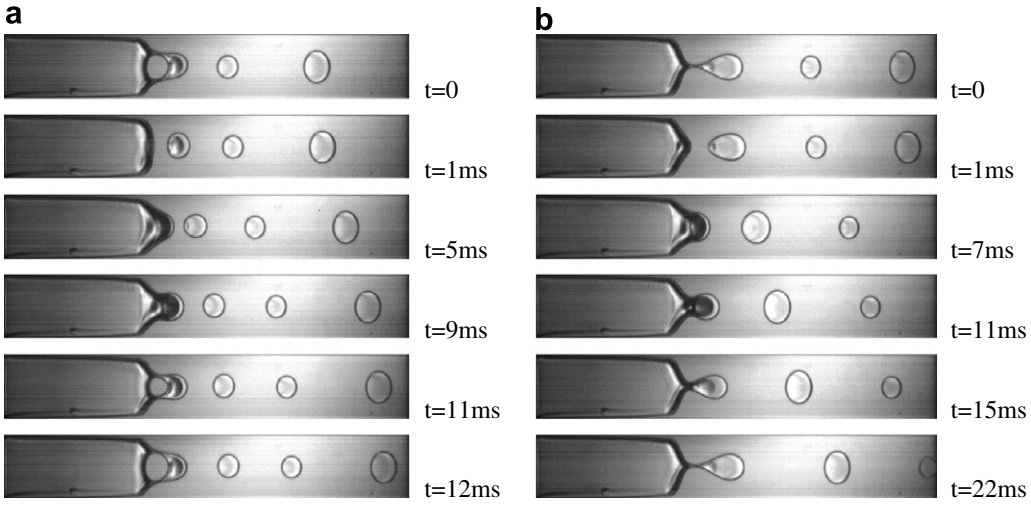

Fig. 5. Video images taken of the two different modes of bubble emission (data from run 2; (a) is the first type and (b) is the second type).

becomes more and more protruded in preparation to emit another bubble. The emitted bubbles form a train which flows downstream in the microchannel. The next bubble breakup clearly starts at $t = 12$ ms (see Fig. 5a) and by $t = 13$ ms the bubble is completely separated (not shown in this figure). Therefore, the cycle period, which is defined as the time needed to form and emit one bubble, is 12 ms. The bubble emission frequency is equal to the inverse of the cycle period, i.e. 83 Hz. The second type of bubble generation mode is shown in Fig. 5b. The cycle period here is 22 ms.

Furthermore, it was possible for the process to alternate between the two modes during the same run. Statistic measurements taken over 35 successive cycles indicated that the cycle period was in the range from 10 to12 ms for the first mode and from 20 to 22 ms for the second mode. Fig. 6a and b show the cycle period fluctuation between the two modes. For the 35 cycles shown, the occurrence probability covered 68% for the first mode and 32% for the second mode.

Fig. 7 shows variation in the ellipsoidal bubble shape after its generation. At $t = 0$ the bubble has just been fully released from the elongated bubble. Initially, the bubble has a horizontal elliptical shape with $D_x > D_y$, but becomes circular at $t = 3$ ms ($D_x = D_y$), and then finally it obtains a vertical elliptical shape ($D_x < D_y$) at $t = 15$ ms. Thus, it takes a total of 15 ms for the bubble shape to stabilize. After 15 ms, the bubble shape and size then remain unchanged but the final shape is influenced by inertia, surface tension and viscosity forces acting on the bubble.

Bubble motion is tracked along the channel using the center or "O" point (see Fig. 4). A plot of bubble displacement versus time in the x and y axes is shown in Fig. 8 for runs 1 and 2. The displacement curve displays a linear relationship with respect to time, indicating that speed along the flow direction (x axis) is constant (see Fig. 8a and b) without any noticeable motion along the y axis (see Fig. 8c). The computed velocities are 7.77 and 6.51 cm/s for run 1 and 2, respectively (Fig. 8b). A constant bubble velocity is an indication of a uniform pressure gradient along the flow direction. A slight higher inlet pressure such as run 2 results in a larger bubble emission frequency and a higher statistic vapor mass quality at the microchannel exit. A limit case is that the flow converts to the annular flow pattern when the inlet pressure is sufficient high (see run 6 in Fig. 3). Thus the liquid flow rate downstream of the elongated bubble is decreased for higher inlet pressure, reducing the viscous force applied on the emitted bubble and a slight slower bubble traveling velocity is obtained downstream of the central microchannel for run 2 than that for run 1.

3.3. Flow pattern with forced convection by flowing water in the copper heat sink

The cooling rate was found to strongly influence the shape and size of the emitted bubbles. For cooling by

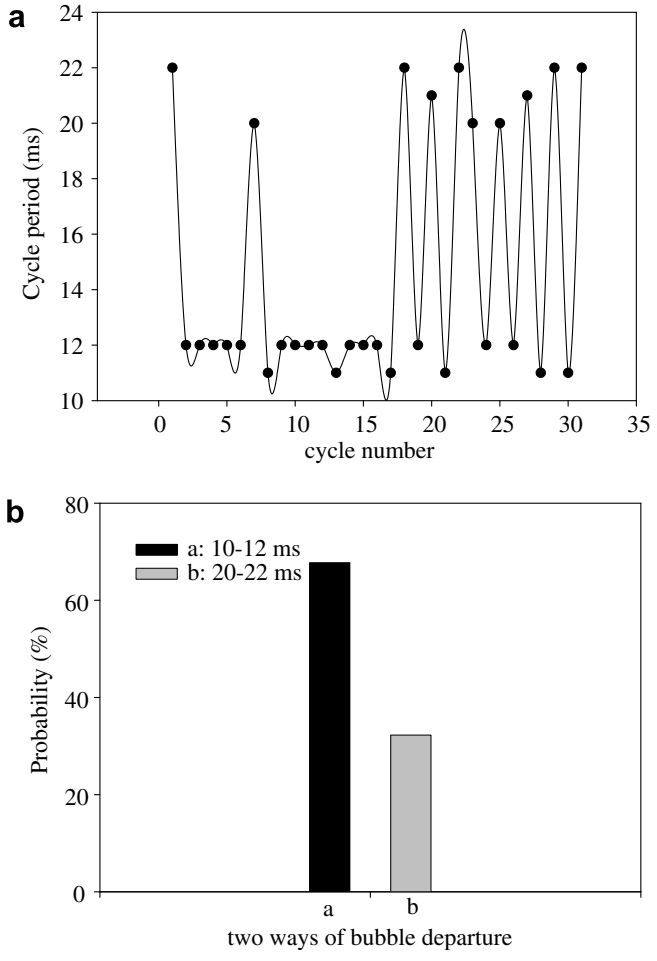

Fig. 6. Alternation between the two types of bubble emission modes: (a) cycle period versus number of occurrences and (b) probability of occurrence of each type of bubble emission mode (run 2).

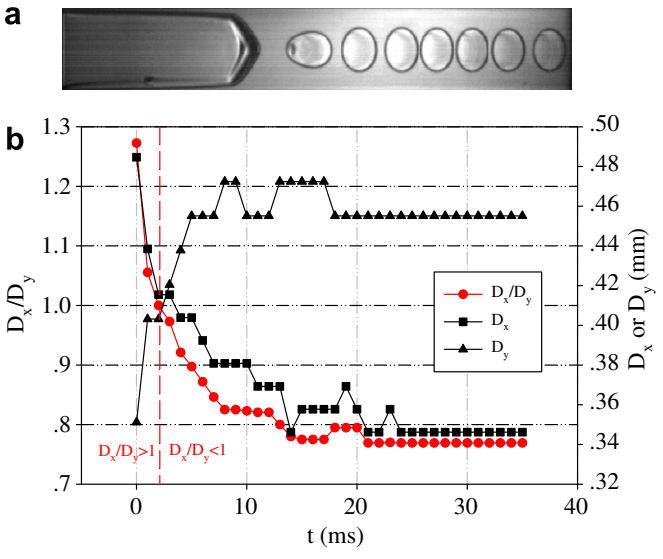

Fig. 7. Transient elliptical bubble shape and size after full separation from the elongated bubble (run 2): (a) video image of a single emitted bubble at different time and (b) plot of D_x/D_y, D_x, and D_y versus time of the run.

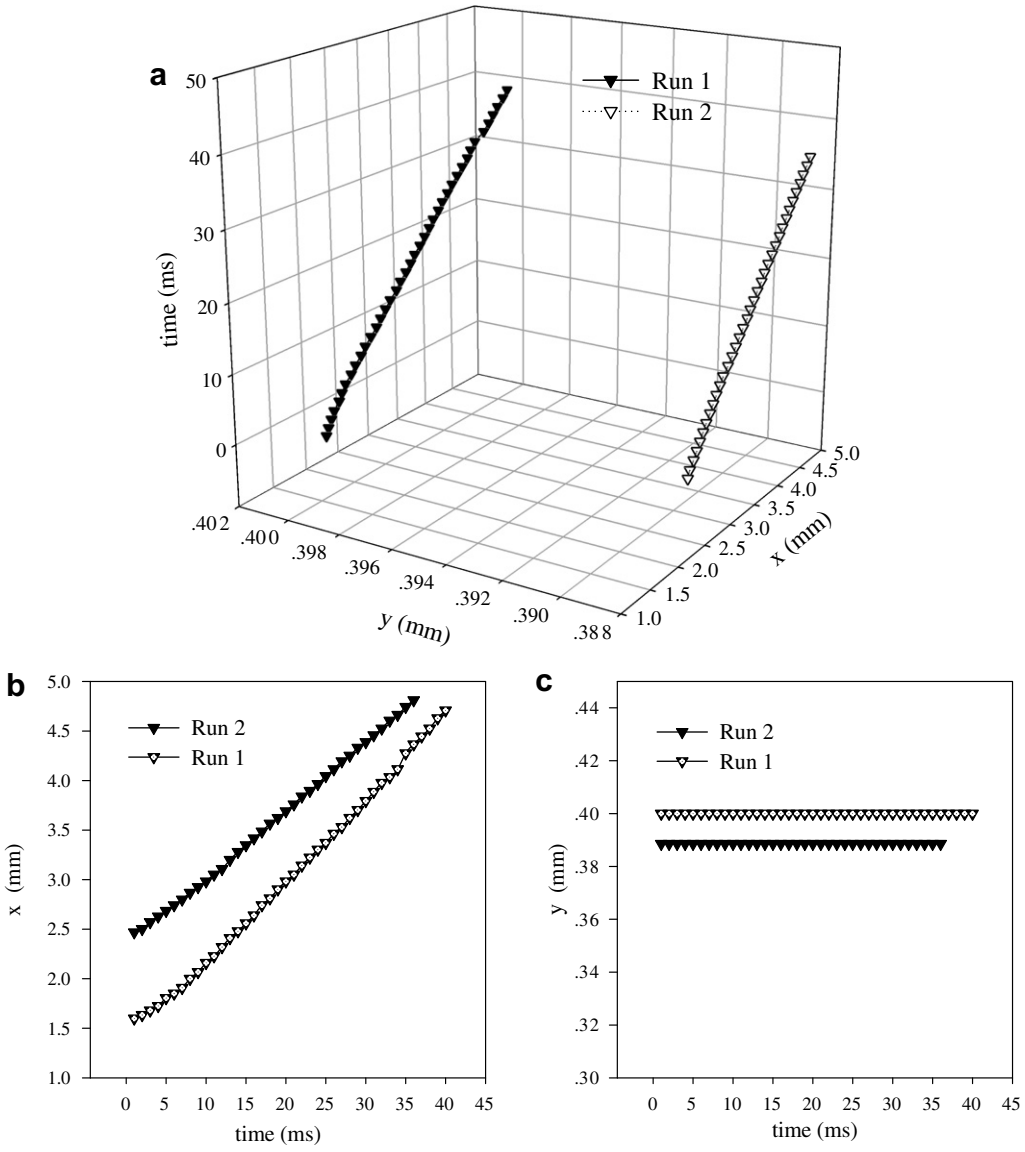

Fig. 8. Displacement of an emitted elliptical bubble in three-dimensions (a) and two-dimensions; (b) x-axis and (c) y-axis for runs 1 and 2.

chilled water flow, the transient process is similar to the natural air convection cooling case, except that: (1) the elongated bubble is shorter for the same inlet steam pressures, (2) the bubble shape is not modified after its generation, (3) the emitted (completely separated) bubble is circular in shape and much smaller, and (4) the bubble emission frequency is larger.

As shown in Fig. 9 for run 21, a tiny bubble is being emitted at $t = 0$ and a new bubble is formed and completely detaches at $t = 0.25$ ms. As the second bubble is emitted at $t = 2.5$ ms, the cycle period is 2.5 ms and thus the emission frequency is 400 Hz.

The emitted circular bubbles form a very well ordered bubble sequence or train with bubbles uniformly distributed along the microchannel centerline. Figs. 10 and 11 show data on bubble sizes and displacements for runs 21, 22, 23 and 24 (see Fig. 3 for operation parameters). As

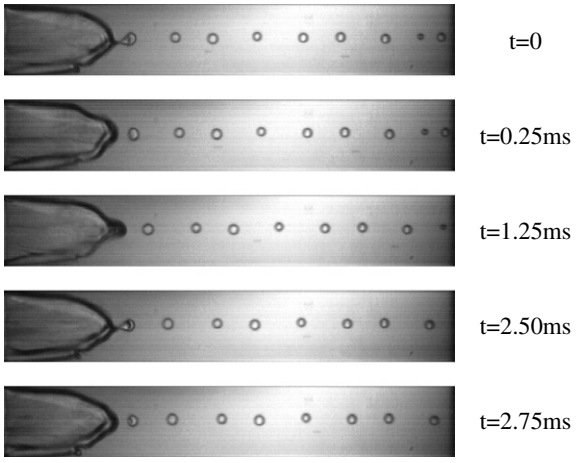

Fig. 9. Video images of periodic bubble emission and ordered bubble sequence (train) flow for run 21.

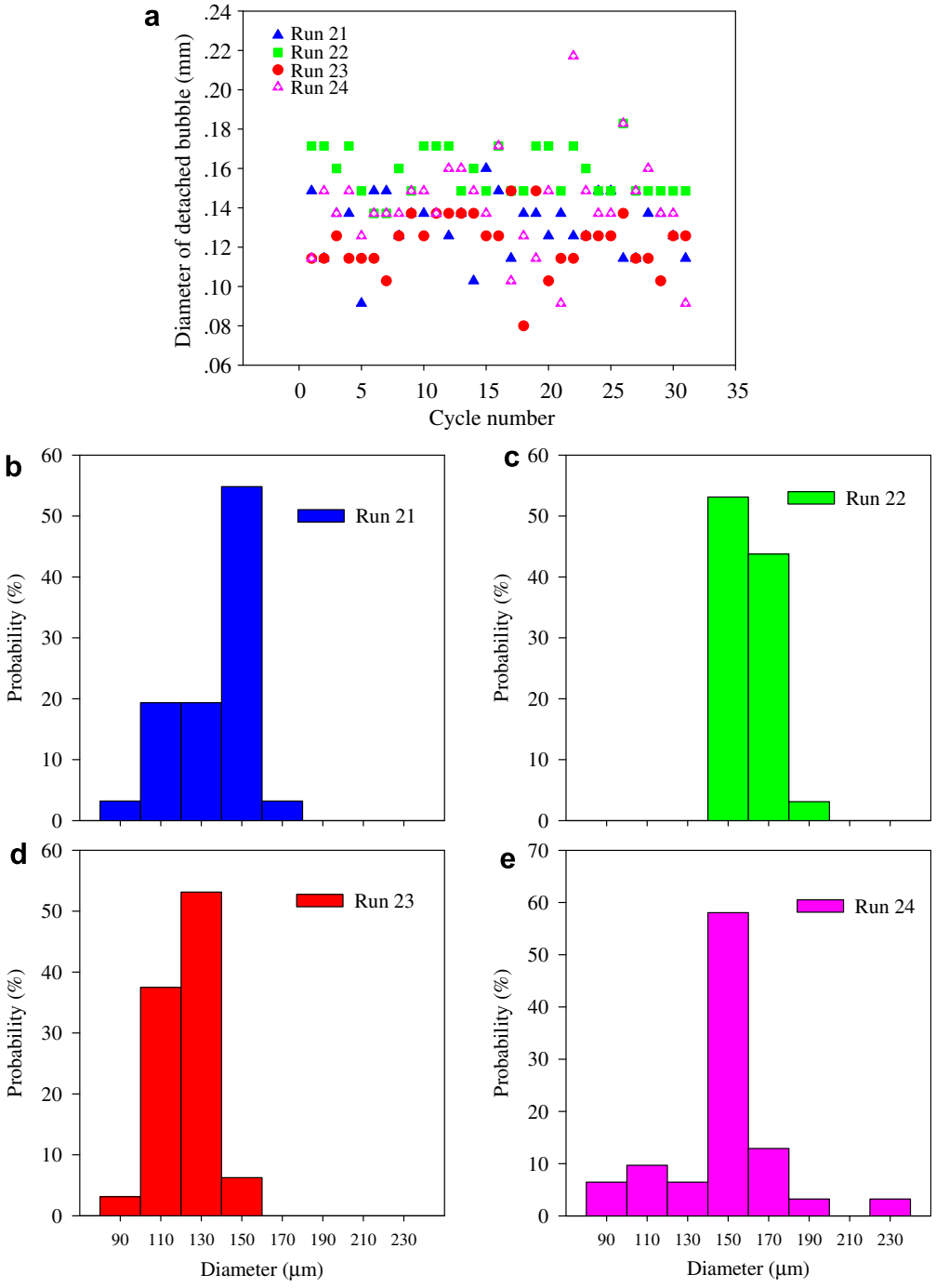

Fig. 10. Emitted bubble size and probability of occurrence for successive cycles at different inlet pressures.

shown in Fig. 10, the emitted bubbles have diameters in the range from 80 to 180 μm for all four runs selected. The largest number of bubbles (more than 50%) have diameters falling in the range from 140 to 160 μm for runs 21, 22 and 24 and in the range from 120 to 140 μm for run 23. The average bubble diameters are 132, 156, 117 and 142 μm with corresponding variances of 18, 11, 13 and 25 μm for runs 21, 22, 23, and 24, respectively.

Similar statistical analysis was performed on the data from cycle periods ranging from 0.5 to 4.75 ms (corresponding to bubble emission frequencies of 210–2000 Hz) for the same four runs. The largest number of cycle periods fall in the range from 1.75 to 2.25 ms for runs 21 and 22 and in range from 1.25 to 1.75 ms for runs 23 and 24. The average cycle periods are 2.26, 2.15, 1.42, and 1.62 ms with corresponding variances of 0.50, 0.60, 0.29, and 0.73 ms for runs 21, 22, 23, and 24, respectively. Bubble displacement versus time for the four runs shows a linear relationship, as shown in Fig. 11, indicating that the bubble translation velocity is constant. For the bubbles

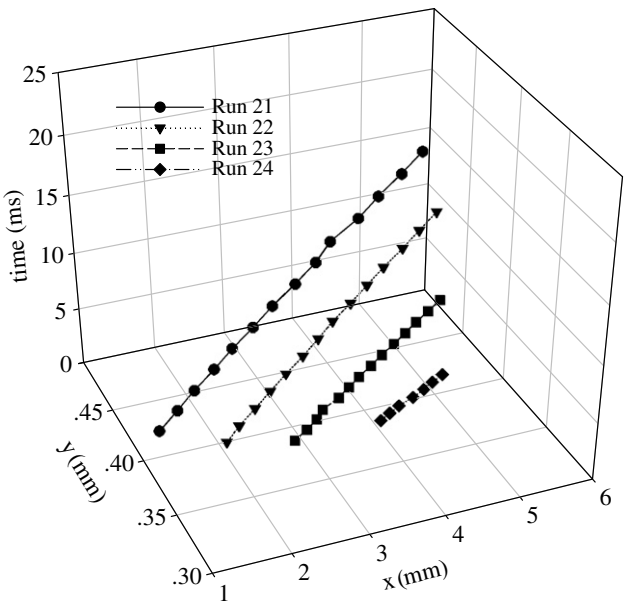

Fig. 11. Bubble displacements in three-dimensions for runs 21, 22, 23 and 24.

analyzed for these four runs their velocities are 18.28, 17.30, 20.04, and 28.19 cm/s.

3.4. Mechanism of periodic bubble emission and ordered bubble sequence (train)

Fig. 12 shows the elongated bubble structure and the detaching bubble in the microchannel. Dry vapor is inside and a continuous liquid is outside of the elongated bubble, that latter formed by the condensation process at the surface of the elongated bubble. The interface of the elongated bubble is curved to respect the force balance of the Laplace equation (see Fig. 12 the red interface), which compensates for the larger pressure inside the elongated bubble.

There exist inertia force and surface tension force on the vapor–liquid interface. The Weber number along the interface is defined as $We = \rho_v(u_v - u_f)^2 D/\sigma_f$, where ρ_v is the vapor density, D is the hydraulic diameter of the microchannel, u_v and u_f are the velocities of the vapor and condensed water, σ_f is the surface tension force of the condensed water along the interface, respectively. The Weber number represents the inertia force relative to the surface tension force. When the Weber number is sufficiently high, the breakup of vapor–liquid interface will take place. We perform our analysis by assuming the axial velocity of the vapor inside the elongated bubble is u, which has a profile across the channel width direction of $u = -\frac{1}{2\mu_v}\frac{dp}{dx}(wy - y^2)$, where $\frac{dp}{dx}$ is the axial pressure gradient inside the elongated bubble and w is the width of the central microchannel. It is clearly seen from the vapor velocity analysis that the center of the vapor–liquid interface has the largest velocity. On the other hand, the condensation flow in the microchannel yields a slight high fluid temperature at the center of the microchannel than that at the side of the microchannel in the channel width direction. Assuming the fluid temperature difference between the center and side of the microchannel is only 1 °C, such small temperature difference leads to a large temperature gradient of 2500 K/m across the channel width direction, highlighting the surface tension force gradient of water in the channel width direction. The surface tension of water is smaller at the microchannel center. The combined effects of the larger vapor velocity and slight smaller surface tension force at the microchannel center always yield the largest Weber number at the microchannel center. This is the reason why the breakup of the upstream elongated bubble always takes place at the center of the microchannel. Covering the data range in the present study, the Weber number is in the range from 100 to 1000, indicating that the inertia force is sufficiently higher than the surface tension force, leading to the breakup of the vapor–liquid interface at the elongated bubble front.

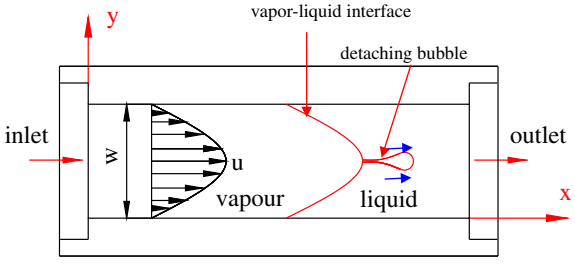

Fig. 12. Schematic diagram shows the vapor velocity distribution inside the elongated bubble, the blue arrows show the direction of the shear force applied on the vapor bubble, causing the bubble to detach from the tip of the elongated bubble (For interpretation of the references in colour in this figure legend, the reader is referred to the web version of this article).

Once the vapor–liquid interface breaks up, the vapor will be discharged from the breakup point, leading to the formation of the protruding vapor bubble. Due to the vapor mass transportation from the elongated bubble to the protruding bubble, the protruding bubble gets larger gradually. As the protruding bubble grows up, the shear force applied on the vapor bubble surface becomes larger due to the expanding surface area, which eventually leads to the vapor bubble breaking off from the elongated bubble under the condition that the shear force is larger than the surface tension force. Once a new bubble is fully separated from the mother elongated bubble, the next cycle begins, leading to a cyclic formation of small bubbles at the tip of the elongated bubble.

The bubble size remains constant after its release from the tip of the elongated bubble. Because the bubbles have a flattened biscuit-shape, there is no model or correlation available which can be used to determine the local condensation heat transfer coefficients at the interface of these bubbles. Therefore, we treat these flattened bubbles being spherical in shape. In that case, bubble condensation in subcooled liquids is controlled either by inertia or by heat diffusion. For high subcoolings, bubbles rapidly collapse satisfying the Rayleigh solution. On the other hand, if the

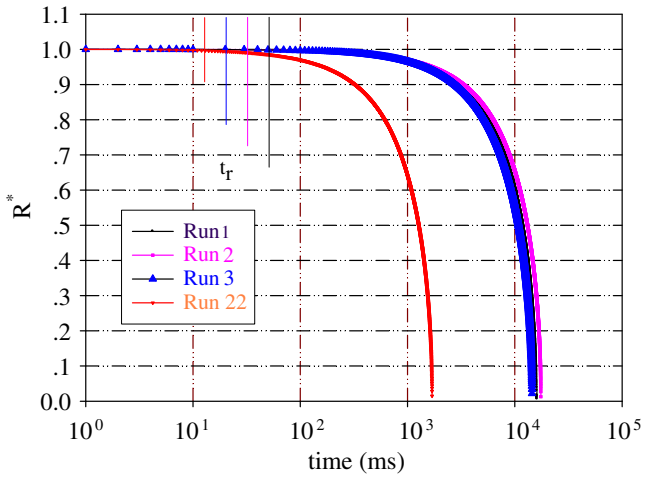

Fig. 13. Reduced equivalent bubble radius, R^*, plotted versus time (The reduced equivalent bubble diameter is computed using calculations reported in [16,17]).

subcooling is low, bubble collapse takes longer and the process is governed by diffusion of the latent heat away from the interface. As noted by Vasil'el [16] and Kalman and Mori [17], the ratio of the Peclet to Jakob number (Pe/Ja) determines the heat transfer mechanism where $Pe/Ja \gg 1$ leads to bubble condensation. On the other hand, inertia dominates if $Pe/Ja \ll 1$. Both mechanisms are important if $Pe/Ja \sim 1$. For the present case the subcooling is low, so heat diffusion at the interface dominates.

The transient non-dimensional bubble radius, R^*, is calculated using the equation $R(t)/R_o$, where R_o is the initial equivalent bubble radius which is determined from $\frac{4}{3}\pi R_o^3 = \pi R_{o,cir}^2 \delta$. $R_{o,cir}$ is the biscuit-shaped bubble radius observed in the xy plane by the optical system and δ is the channel depth of 30 μm. The correlation $Nu = 0.0041(Pe)^{0.855}$ [17] is used to compute the condensation heat transfer. This correlation works well for $0.05 < Re < 2000$ and $10 < Pe < 20000$. A plot of R^* versus time is shown in Fig. 13. The bubble residence times in the microchannel have been measured from the video images and are also indicated in Fig. 13. The time at which R^* approaches zero is called the "bubble collapse" time. It was found that the bubble residence time, ranging from 10 to 100 ms, is at least two orders of magnitude less than the bubble collapse time, which ranges from 1000 to 10,000 ms. Therefore, during the bubble residence time in the microchannel, the bubble radius changes very little and thus the bubble size remains nearly constant. The uniform bubble size along with the constant bubble generation frequency gives rise to the ordered bubble sequence (train) seen in the microchannel videos.

4. Conclusions

A study of condensation flow in a single silicon microchannel with a depth of 30 μm has been reported here. The micro-condenser studied consisted of inlet and outlet plenums and a single microchannel. Such a configuration led to the formation of a stable elongated bubble attached at the microchannel upstream followed by a train of small bubbles which detached from that elongated bubble periodically and flowing downstream to the outlet. The bubble train is a sequence of isolated bubbles with uniform size and velocity which are periodically generated from the tip of the elongated bubble.

It was found that the cooling rates strongly affected the bubble parameters, such as size, shape and generation frequency. Higher cooling rates achieved with forced convection via flowing chilled water in the copper heat sink increased the bubble generation frequency and decreased the bubble size. The larger Weber number at the centerline of the microchannel results in the breakup of the vapor–liquid interface, and the vapor is released from the breakup point at the elongated bubble front, forming the protruding vapor bubble. The increasing shear force applied on the vapor bubble due to the expanding bubble surface area contributes to the breaking off the protruded vapor bubble.

The bubble size remained nearly constant in the microchannel after its emission due to the fact that the bubble residence time in the microchannel is two orders of magnitude smaller than the computed bubble collapse time. The reported experimental results could be exploited to develop a method for creating bubbles of controlled size and frequency on the microscale for microfluidic applications.

Acknowledgements

This work was supported by the Natural Science Foundation of China (50776089) and the Natural Science Foundation of Guangdong Province (7000742). The authors thank Prof. Dacheng Zhang and Ms. Fang Yang (Institute of Microelectronics, Peking University, China) for fabricating the silicon micro-condenser.

References

[1] S. Garimella, J.D. Killion, J.W. Coleman, An experimentally validated model for two-phase pressure drop in the intermittent flow regime for circular microchannels, J. Fluid Eng. Trans. ASME 124 (1) (2002) 205–214.
[2] S. Garimella, A. Agarwal, J.D. Killion, Condensation pressure drop in circular microchannels, Heat Transfer Eng. 26 (3) (2005) 28–35.
[3] J.R. Baird, D.F. Fletcher, B.S. Haynes, Local condensation heat transfer rates in fine passages, Int. J. Heat Mass Transfer 46 (23) (2003) 4453–4466.
[4] H.S. Wang, J.W. Rose, H. Honda, A theoretical model of film condensation in square section horizontal microchannels, Chem. Eng. Res. Des. 82 (A4) (2004) 430–434.
[5] B. Médéric, P. Lavieille, M. Miscevic, Void fraction invariance properties of condensation flow inside a capillary glass tube, Int. J. Multiphase Flow 31 (2005) 1049–1058.
[6] A. Cavallini, D. Del Col, L. Doretti, M. Matkovic, L. Rossetto, C. Zillo, Two-phase frictional pressure gradient of R236ea, R134a and R410a inside multiport minichannels, Exp. Therm. Fluid Sci. 29 (7) (2005) 861–870.
[7] T.M. Bandhauer, A. Agarwal, S. Garimella, Measurement and modeling of condensation heat transfer coefficients in circular

microchannels, J. Heat Transfer Trans. ASME 128 (10) (2006) 1050–1059.
[8] X.Z. Du, T.S. Zhao, Analysis of film condensation heat transfer inside a vertical micro tube with consideration of the meniscus draining effect, Int. J. Heat Mass Transfer 46 (24) (2003) 4669–4679.
[9] H.S. Wang, J.W. Rose, A theory of film condensation in horizontal noncircular section microchannels, J. Heat Transfer Trans. ASME 127 (10) (2005) 1096–1105.
[10] H.S. Wang, J.W. Rose, Film condensation in horizontal microchannels, Int. J. Therm. Sci. 45 (12) (2006) 1205–1212.
[11] H.Y. Wu, P. Cheng, Condensation flow patterns in silicon microchannels, Int. J. Heat Mass Transfer 48 (2005) 2186–2197.
[12] J. Mathieu, A. Armand, Droplet control for microfluidics, Science 309 (2005) 887–888.
[13] H.A. Stone, A.D. Stroock, A. Ajdari, Engineering flows in small devices: microfluidics toward a lab-on-a-chip, Annu. Rev. Fluid Mech. 36 (2004) 381–411.
[14] D. Huh, Y.C. Tung, H.H. Wei, J.B. Grotberg, S.J. Skerlos, Use of air–liquid two-phase flow in hydrophobic microfluidic channels for disposable flow cytometers, Biomed. Microdev. 4 (2002) 141–149.
[15] J.L. Xu, Y.H. Gan, D.C. Zhang, X.H. Li, Microscale boiling heat transfer in a micro-timescale at high heat fluxes, J. Micromech. Microeng. 15 (2005) 362–376.
[16] A.P. Vasil'ev, Dynamics and heat transfer in collapse of a bubble containing wet vapor in hydrophobic liquid, J. Eng. Phys. Thermophys. 76 (4) (2003) 838–846.
[17] H. Kalman, Y.H. Mori, Experimental analysis of a single vapor bubble condensing in subcooled liquid, Chem. Eng. J. 85 (2002) 197–206.